PAPER

Design of highly porous Fe₃O₄@reduced graphene oxide *via* a facile PMAA-induced assembly†

Huan Wang,[a] Madumali Kalubowilage,[b] Stefan H. Bossmann [ID][b] and Placidus B. Amama [ID] *[a]

Advances in the synthesis and processing of graphene-based materials have presented the opportunity to design novel lithium-ion battery (LIB) anode materials that can meet the power requirements of next-generation power devices. In this work, a poly(methacrylic acid) (PMAA)-induced self-assembly process was used to design super-mesoporous Fe₃O₄ and reduced-graphene-oxide (Fe₃O₄@RGO) anode materials. We demonstrate the relationship between the media pH and Fe₃O₄@RGO nanostructure, in terms of dispersion state of PMAA-stabilized Fe₃O₄@GO sheets at different surrounding pH values, and porosity of the resulted Fe₃O₄@RGO anode. The anode shows a high surface area of 338.8 m² g⁻¹ with a large amount of 10–40 nm mesopores, which facilitates the kinetics of Li-ions and electrons, and improves electrode durability. As a result, Fe₃O₄@RGO delivers high specific-charge capacities of 740 mA h g⁻¹ to 200 mA h g⁻¹ at various current densities of 0.5 A g⁻¹ to 10 A g⁻¹, and an excellent capacity-retention capability even after long-term charge–discharge cycles. The PMAA-induced assembly method addresses the issue of poor dispersion of Fe₃O₄-coated graphene materials—which is a major impediment in the synthesis process—and provides a facile synthetic pathway for depositing Fe₃O₄ and other metal oxide nanoparticles on highly porous RGO.

Introduction

Smart or stimuli-responsive polymers are suitable to construct a morphology-controllable network due to their conformation and structural change in response to applied external stimuli such as pH, temperature, light, and electrical or magnetic fields.[1–3] Slight external triggers can induce significant changes in the structure and properties of smart polymers including the change of degree of cross-linking, expansion, or shrinkage of polymer volume, or the detachment of polymer functional groups. Poly(methacrylic acid) (PMAA), a common pH-responsive polymer, has already attracted intense attention due to its interesting dependence of charge density on the solution.[4–6] PMAA contains a large number of ionizable carboxyl groups, which makes it a type of water-soluble weak polyelectrolyte with a pK_a value of 4.9.[7] The dissociation degree of carboxyl groups is largely influenced by the environmental pH; and PMAA chains can undergo reversible transitions between tightly coiled conformations at low pH and highly extended conformations at high pH.[8]

Due to its super electrochemical properties and structural moldability, graphene has emerged as an excellent candidate for replacing commercial graphite anodes in lithium-ion batteries (LIBs).[9] Large scalable preparation of graphene-based electrodes utilize graphene oxide (GO) as a host combining other high capacity metal/metal oxide active materials. Porous 3D graphene architecture[10,11] has been widely developed to accommodate the restacking issue of GO sheets during common fabrication processes. Porous graphene serves as efficient conductive channels and buffer skeleton network, which can facilitate charge transfer and protect other active nanoparticles during the cycling process. Previous zeta-potential analyses[12,13] indicate that GO sheets are negatively charged in aqueous media over a wide pH range of 1 to 11. The charge density of GO varies with pH, enabling GO sheets to also be considered as a pH-responsive material. Recently, some pH-sensitive GO-based materials have been prepared by grafting PMAA polymer *via* covalent or noncovalent interactions.[14,15] In general, prior studies mainly focused on tuning pH-responsive properties of polymer chains for application in biomedical engineering,[2,3] while applications in energy storage, especially LIBs, are yet to be reported.

Fe₃O₄ has a high theoretical capacity of 924 mA h g⁻¹ and is widely used in combination with nanocarbons for designing LIB anodes.[16–18] Fe₃O₄ nanoparticles of controlled size distribution can be deposited onto GO sheets (Fe₃O₄@GO) *via in situ* aqueous reaction, resulting in coordination bonds between Fe atoms and COOH groups on a GO surface.[16] However, the concentration of Fe₃O₄@GO aqueous suspension is usually very low (<0.6 mg ml⁻¹)

*a*Tim Taylor Department of Chemical Engineering, Kansas State University, Manhattan, KS 66506, USA. E-mail: pamama@ksu.edu

*b*Department of Chemistry, Kansas State University, Manhattan, KS 66506, USA

† Electronic supplementary information (ESI) available: Table S1: Surface areas of Fe₃O₄@RGO; Fig. S1: FTIR spectrum of PMAA; Fig. S2: TEM images of Fe₃O₄@RGO; Fig. S3: TGA curve of PMAA; Fig. S4: SEM images of Fe₃O₄@RGO; Fig. S5: TEM image of Fe₃O₄@RGO; Fig. S6: Cycling performance of PMMA-induced and citric acid-stabilized Fe₃O₄@RGO. See DOI: 10.1039/c9ra04980k

due to the reduced number of repelling functional groups after depositing Fe_3O_4 onto a GO surface. The use of PMAA as a stabilizer can result in a higher concentration of Fe_3O_4@GO suspension in water. More importantly, it is possible to control the dispersion state of PMAA-stabilized Fe_3O_4@GO sheets in water by changing the pH, due to the high pH response of PMAA; we emphasize this simple strategy can be employed in the design of high-performance electrode materials for LIB application. Previous studies of developing a desired Fe_3O_4@graphene electrode mainly focused on seeking novel synthesis reactions of a Fe_3O_4@graphene nanocomposite,[19–22] controlling the size of Fe_3O_4 nanoparticles,[23–25] and optimizing structural design of the composites mostly by sacrificial template methods.[18,26,27] However, self-assembly of Fe_3O_4@graphene has received little attention, especially using a pH-responsive polymer as the assembly agent. As mentioned above, in spite of the immense potential of pH-responsive polymers in LIB application, current publications on the subject are limited.[1,2,4,8] As a common pH-responsive polymer, PMAA is worthwhile to investigate in terms of designing the desired Fe_3O_4@GO structure with high porosity and well-dispersed Fe_3O_4 for high-performance anodes. Furthermore, the underlying mechanism of self-assembly behavior of Fe_3O_4@GO sheets using PMAA is poorly understood and will benefit from further examination.

Herein, we report the rational design of highly porous Fe_3O_4@RGO anodes *via* a facile PMAA-induced self-assembly method that involves adjusting the pH of the aqueous media. Synthesis steps for porous Fe_3O_4@RGO anodes are illustrated in Fig. 1. Fe_3O_4@GO sheets form a network and PMAA acts as a stabilizer, a cross-linking agent, and a driving force for structural change. The Fe_3O_4@GO–PMAA sheets demonstrate phase transfer behavior at different pH since PMAA is a weak polyanion, exhibiting a negative and neutral charge at high and low pH, respectively.[4–6] The study also evaluates the effectiveness of PMAA in dispersing Fe_3O_4@GO in water and probes the pH-responsive behavior of the stabilized suspensions. Various techniques (rheology measurement, UV-Vis, electron microscopy, and electrophoretic light scattering) were used to characterize the dispersion of Fe_3O_4@GO.[16,20,21,28,29] The results indicate that PMAA is influential in controlling the dispersion state of Fe_3O_4@GO in water, and the resulting porosity of Fe_3O_4@RGO after drying and annealing. Furthermore, lower weight ratio of PMAA to Fe_3O_4@GO shows different degrees of stabilization of Fe_3O_4@GO in comparison to the same sample with the same pH solution, but with a higher weight ratio. Based on the results, a stabilizing mechanism is proposed to explain the pH-responsive self-assembly of Fe_3O_4@GO sheets in water. This work provides fresh insights into the dispersion and stabilization of Fe_3O_4@GO in water using weak polyelectrolytes and a novel synthetic pathway for controlled fabrication of super-mesoporous Fe_3O_4@RGO composites. The PMAA-induced self-assembly method addresses the issue of poor dispersion of Fe_3O_4-coated graphene materials—which is a major challenge during synthesis of graphene-based nanocomposites—and provides a new and facile synthetic pathway for producing highly porous RGO framework that serve as a support for well-dispersed Fe_3O_4 or other metal oxide nanoparticles.
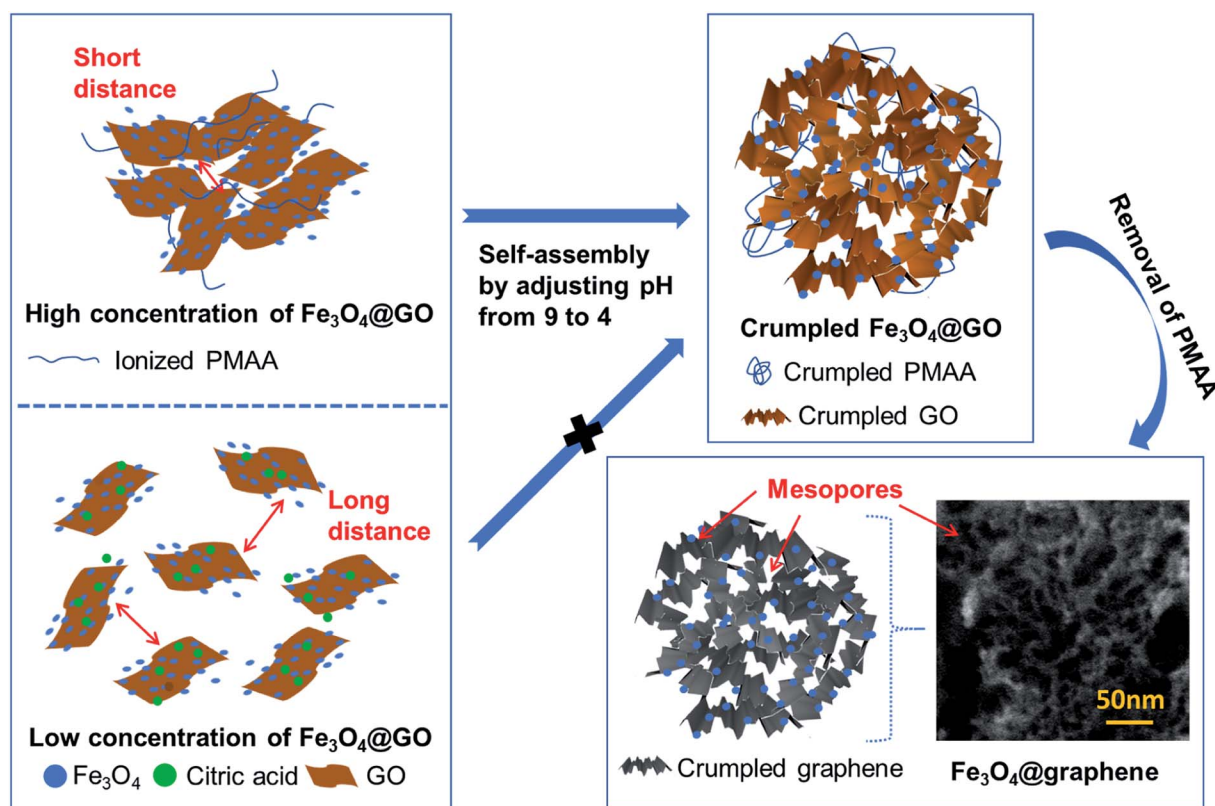

Fig. 1 Schematic illustration of self-assembly of crumpled Fe_3O_4/RGO anodes *via* adjusting pH of dispersion.

Results and discussion

pH-Response of Fe₃O₄@GO–PMAA in aqueous dispersion

Fig. 2a shows the molecular structures of citric acid and PMAA. The COOH groups on both molecules can form coordinative bonds with Fe_3O_4, and thus can be used as stabilizers for Fe_3O_4@GO dispersion. However, citric acid is a much smaller molecule than the long-chain PMAA polymer, which makes citric acid a type of non pH-sensitive electrolyte. The FTIR spectrum (Fig. S1†) shows strong characteristic wide absorption peaks around 3000 cm^{-1} that are associated with COOH groups on the PMAA chains. The conformational changes the PMAA chain undergoes as a function of pH is schematically shown in Fig. 2b, which are consistent with previous research publications.[5,8,30] PMAA is a type of weak polyacid with isoelectric point at pH ∼ 2.[30]

Therefore, PMAA can form a transparent and homogeneous water solution (1.2 mg ml^{-1} and 4.8 mg ml^{-1}) at any pH higher than 1.0 due to ionization of COOH associated with negative zeta potential values.[30] At high pH (>5), the PMAA chains are in an ionized state and behave as a randomly coiled or extended configuration. The high negative-charge density along the polymer backbone causes the polymer chain to repel itself, and thus further stabilize the attached Fe_3O_4@GO sheets. At low pH (<4), PMAA exhibits significant intramolecular hydrogen bonding, resulting in a more crumpled or globular-like conformation. A previous study[5] confirmed that sudden conformational change of PMAA occurs from a collapsed conformation to a random coil in the range of pH 4–6.

PMAA can generally stabilize Fe_3O_4@GO sheets in water media at pH between 5 and 9, as shown by the pictures of PMAA aqueous solutions and Fe_3O_4@GO–PMAA suspensions in Fig. 3; a summary of their dispersion states is presented in Table 1. Two PMAA aqueous solutions with 1.2 mg ml^{-1} and 4.8 mg ml^{-1} were used for this study. The black Fe_3O_4@GO suspensions were stable even after storing for a long time (>1 month). However, at pH <4 or >9, the Fe_3O_4@GO sheets are highly aggregated. Note at specific pH (pH 5, 7, and 9), there are differences in the degree of dispersion for Fe_3O_4@GO stabilized by 1.2 mg ml^{-1} PMAA and 4.8 mg ml^{-1} PMAA. The stability of Fe_3O_4@GO dispersion with 4.8 mg ml^{-1} PMAA decreases from "highly dispersed" to "moderately dispersed", and then to "slightly dispersed" with increasing pH from 5 to 7 and then to 9, respectively. In particular, at pH 9, some particles in Fe_3O_4@GO dispersion with 4.8 mg ml^{-1} PMAA can be observed at the bottom of the container after one month of storage; whereas for Fe_3O_4@GO dispersion with 1.2 mg ml^{-1} PMAA, the best stability was achieved at pH 7, and dispersions at pH 5 and 9 exhibited moderate stabilities.

To rationalize the observed difference in the stability of the dispersions at pH 5, 7, and 9, zeta potential, UV-Vis spectroscopic and viscosity measurements were carried out. Zeta potential represents the equilibrium electric potential at the shear plane (or slip plane) of particles in a liquid.[31,32] Typically, the more positive or negative zeta potentials correspond to higher stability of dispersed particles. Table 2 shows zeta potentials for Fe_3O_4@GO–PMAA aqueous suspensions with 1.2 mg ml^{-1} and 4.8 mg ml^{-1} PMAA at pH 5, 7, and 9. The zeta potential exhibits an increasing trend with pH from 5 to 9, regardless of the concentration of PMAA; this is mainly attributed to the increasing amount of COOH groups ionized from PMAA as the pH increases. Besides, at the same pH, 4.8 mg ml^{-1} PMAA-stabilized Fe_3O_4@GO suspensions show higher zeta potentials than those with 1.2 mg ml^{-1} PMAA. Interestingly, even though the most negative zeta potential occurs at pH 9 for the Fe_3O_4@GO–PMAA suspensions at various concentrations, the highest stabilities were observed at much lower pH (pH 5 for 4.8 mg ml^{-1} PMAA-stabilized Fe_3O_4@GO and pH 7 for 1.2 mg ml^{-1} PMAA-stabilized Fe_3O_4@GO). This 'paradox' has been explained by UV-Vis spectroscopic and particle-size data presented in the following discussion.

UV-Vis spectroscopic analysis was used to determine the optimum pH for stabilizing Fe_3O_4@GO (Fig. 4a). The stability of 2 mg ml^{-1} Fe_3O_4@GO with 1.2 mg ml^{-1} PMAA and 4.8 mg ml^{-1} PMAA dispersions were systematically studied at different pH. After diluting and resting the aforementioned dispersions for four days, the upper stable dispersions were tested in order to minimize the scattering influence of agglomerated particles on
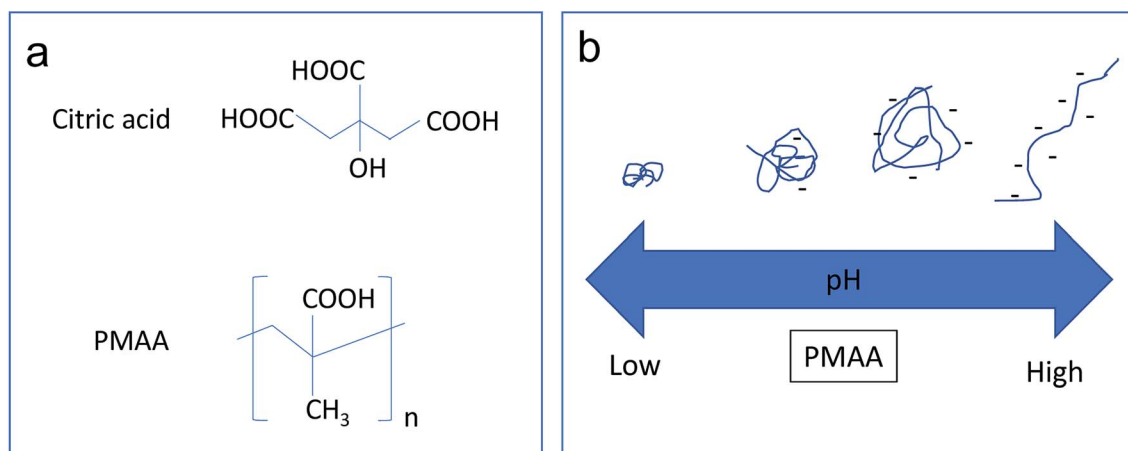

Fig. 2 (a) Structure of citric acid and PMAA. (b) Schematic illustration of the effect of pH on the chain conformations of PMAA.

Fig. 3 Pictures of PMAA aqueous solution and Fe$_3$O$_4$@GO aqueous suspensions stabilized with 1.2 mg ml^{-1} and 4.8 mg ml^{-1} PMAA at different pH levels.

increasing UV absorbance. It has been reported that suspensions containing more dispersed particles have higher UV absorbance compared to suspensions containing agglomerated ones.[8,33] An amount of 1.2 mg ml^{-1} PMAA-stabilized Fe$_3$O$_4$@GO at pH 7 shows the highest UV-Vis absorption, while for 4.8 mg ml^{-1} PMAA-stabilized Fe$_3$O$_4$@GO, the highest absorption occurs at a pH of 5. Since pure PMAA (1.2 or 4.8 mg ml^{-1}) shows almost zero UV-Vis absorbance, the mentioned difference in the UV-Vis absorption may be due to the presence of more COO$^-$ in 4.8 mg ml^{-1} PMAA-stabilized Fe$_3$O$_4$@GO sheets than in 1.2 mg ml^{-1} PMAA-stabilized Fe$_3$O$_4$@GO, which has been verified by the zeta potential data in Table 2. So, for 4.8 mg ml^{-1} PMAA-stabilized Fe$_3$O$_4$@GO, at a relatively lower pH of 5, there is enough negative-charge density (-36.5 mV of zeta potential) along the GO sheet for repulsing other neighboring GO sheets,

Table 2 Zeta potential of Fe$_3$O$_4$@GO–PMAA aqueous suspensions with 1.2 mg ml^{-1} and 4.8 mg ml^{-1} PMAA at different pH levels

pH	Zeta potential (mV)	Zeta potential (mV)
5	-21.4	-36.5
7	-26.9	-48.5
9	-51.1	-52.9
$T = 23\,^\circ$C	1.2 mg ml^{-1a}	4.8 mg ml^{-1a}

^{a} Concentration was diluted to one-half of original concentration for testing.

even though PMAA are still in coiled conformation at that acidic pH. In comparison, for 1.2 mg ml^{-1} PMAA-stabilized Fe$_3$O$_4$@GO, enough charge density can be achieved at pH 7

Table 1 Dispersion state of PMAA aqueous solution and Fe$_3$O$_4$@GO–PMAA aqueous suspensions with 1.2 mg ml^{-1} and 4.8 mg ml^{-1} PMAA at different pH levels

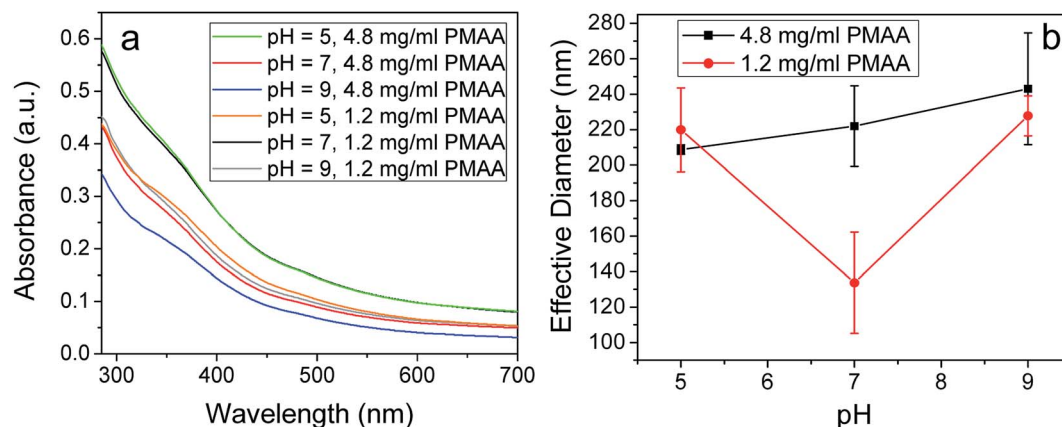| pH	PMAA dispersion	pH	Fe$_3$O$_4$@GO dispersion (1.2 mg ml^{-1} PMAA)	Fe$_3$O$_4$@GO dispersion (4.8 mg ml^{-1} PMAA)
1	Precipitated	1–3	Precipitated	Precipitated
2–3	Mostly crumbled	4	Slightly dispersed	Slightly dispersed
4–6	Crumpled to coiled	5	Moderately dispersed	Highly dispersed
7	Mostly coiled	7	Highly dispersed	Moderately dispersed
9–11	Mostly extended	9	Moderately dispersed	Slightly dispersed
		11	Precipitated	Precipitated

Fig. 4 (a) UV-Vis spectra of Fe_3O_4@GO–PMAA aqueous suspensions with 1.2 mg ml^{-1} and 4.8 mg ml^{-1} PMAA at different pH levels. (b) Effective particle diameter of PMAA-stabilized Fe_3O_4@GO aqueous suspensions with 1.2 mg ml^{-1} and 4.8 mg ml^{-1} PMAA at different pH levels.

(−26.9 mV of zeta potential) instead of at pH 5 (−21.4 mV of zeta potential). As pH increases from 5 to 9, more carboxylate groups emerge, resulting in a fully extended configuration of PMAA chains formed eventually. Note that it is highly possible that one extended PMAA chain attaches to more than one surrounding GO sheet *via* bonding with Fe_3O_4; as a result, the GO sheets can be pulled much closer, resulting in restacking. Ditsch *et al.*[34] reported a similar phenomenon for the poly acrylic acid (PAA)-stabilized Fe_3O_4, demonstrating that one PAA chain can link to multiple Fe_3O_4 particles and then form 'bridges' between Fe_3O_4 particles. For 4.8 mg ml^{-1} PMAA-stabilized Fe_3O_4@GO, UV-Vis absorption decreases as pH increases from 5 to 9; this result supports the 'bridging'-induced restacking hypothesis at high pH range. Interestingly, the UV-Vis absorption profiles for 1.2 mg ml^{-1} PMAA stabilized Fe_3O_4@GO are somewhat different at different pH. We conclude from the results that enough charge density of PMAA cannot be achieved at pH 5, but can be at pH 7, and thus the highest absorption occurs at pH 7; whereas at pH 9, the restacking of GO sheets also occurs, albeit insignificantly, compared to that of 4.8 mg ml^{-1} PMAA-stabilized Fe_3O_4@GO.

Size of Fe_3O_4@GO–PMAA in Fig. 4b supports the 'bridging' phenomenon observed in the UV-Vis data. DLS technology was used here to observe mean effective particle diameter (z-average diameter) and standard size deviations of Fe_3O_4@GO–PMAA. The smallest effective particle diameter was achieved at pH 7 for the 1.2 mg ml^{-1} PMAA-stabilized Fe_3O_4@GO, which suggests the optimum dispersion state under these conditions, while the particle size increases at pH 5 due to the lower charge density on Fe_3O_4@GO sheets. At pH 9, even though the charge density reaches a high value (−51.1 mV of zeta potential), the stability of the suspension decreases because of the 'bridge' between neighboring Fe_3O_4@GO sheets. In comparison, for the 4.8 mg ml^{-1} PMAA-stabilized Fe_3O_4@GO, the effective particle diameter keeps increasing from pH 5 to 9. The most severe 'bridging' occurs at pH 9, which results in a slightly dispersed suspension, as observed in Fig. 3. TEM images (Fig. S2†) also support that at pH 9, 4.8 mg ml^{-1} PMAA-stabilized Fe_3O_4@GO sheets suffer severe agglomeration; unlike an extended sheet-like structure, flower-shaped patterns of

Fe_3O_4@GO sheets were induced by the bridging effect at high PMAA concentration. Given that at pH 9, particles in 4.8 mg ml^{-1} PMAA-stabilized Fe_3O_4@GO experience slight aggregation during the DLS (dynamic light scattering) testing,[29] we performed testing for shorter duration (<10 seconds) to determine the correct effective particle diameter for this sample. Therefore, based on the UV-Vis and particle-size results, we conclude that in general, Fe_3O_4@GO suspensions show better stability at pH 5 or 7 than at pH 9, and the point where 'bridging' occurs is related to the concentration of PMAA (or the weight ratio of PMAA to Fe_3O_4@GO).

Suspensions with well-dispersed GO sheets are known to show higher viscosities compared to those that have agglomerated sheets.[35] Furthermore, it was shown that below the critical concentration of 90 mg ml^{-1}, PMAA–water solution does not show shear thinning or thickening behavior with an increase of shear rate.[36] The observed shear-thinning behavior in Fe_3O_4@GO–PMMA suspensions suggests the presence of highly dispersed Fe_3O_4@GO sheets. In an effort to investigate this pH-dependent behavior, viscosity measurements were obtained for 1.2 mg ml^{-1} and 4.8 mg ml^{-1} PMAA-stabilized Fe_3O_4@GO aqueous suspensions (Fig. 5) at pH 5 and 7. The concentration of PMAA polymer denominates the viscosity of suspension due to the sticky nature of polymer. In general, 4.8 mg ml^{-1} PMAA-stabilized Fe_3O_4@GO suspensions show higher viscosity compared to those of 1.2 mg ml^{-1} PMAA-stabilized Fe_3O_4@GO suspensions. The similar viscosities at pH 5 and 7 for 4.8 mg ml^{-1} PMAA-stabilized Fe_3O_4@GO also reveal the bigger influence of PMAA concentration on viscosity, although the dispersion state at pH 5 is better than pH 7, based on UV-Vis absorption results. After comparing all viscosity profiles shown in Fig. 5, we conclude again that 1.2 mg ml^{-1} PMAA-stabilized Fe_3O_4@GO at pH 7 and 4.8 mg ml^{-1} PMAA-stabilized Fe_3O_4@GO at pH 5 are the two conditions for the highest dispersion due to their high viscosities.

Chemical and structural characterization of Fe_3O_4@RGO anode

As shown in Fig. 1, Fe_3O_4@RGO anode materials are produced after annealing the Fe_3O_4@GO–PMAA sheets at 600 °C for 3 h. GO sheets

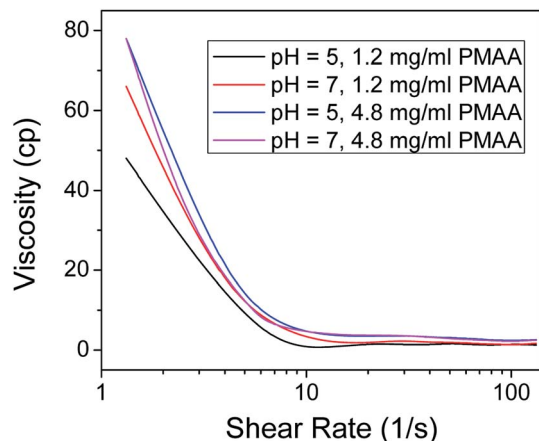Fig. 5 Viscosity as a function of shear rate for $Fe_3O_4@GO$–PMAA aqueous suspensions with 1.2 mg ml^{-1} and 4.8 mg ml^{-1} PMAA at different pH levels.

can be thermally reduced to RGO; meanwhile, PMAA can be removed with only 7 percent residual amorphous carbon (TGA, Fig. S3†). The porous structure of $Fe_3O_4@RGO$ was designed by adjusting the pH of 1.2 mg ml^{-1} PMAA-stabilized $Fe_3O_4@GO$ suspension from 9 to 4. $Fe_3O_4@GO$ sheets were first stabilized by PMAA at pH 9, and under this condition, PMAA chains are completely extended and behave like connecting 'bridges' by linking neighboring $Fe_3O_4@GO$ sheets. Therefore, neighboring GO sheets are constrained by PMAA chains instead of randomly dispersing in water. The distance between GO sheets decreased significantly when compared to that of citric acid-stabilized GO sheets. After decreasing pH from 9 to 4, the PMAA chains shrink to a highly coiled structure and the attached $Fe_3O_4@GO$ sheets are forced to crumple at the same time.

The as-synthesized $Fe_3O_4@RGO$ anode material was analyzed by XRD first (Fig. 6a). Diffraction peaks at $2\theta = 28.9°$, $34.9°$, $42.4°$, $57.8°$, and $62.0°$ are assigned to the (220), (311), (400), (511) and (440) planes of face-centered cubic Fe_3O_4 (JCPDS No. 63-3107), respectively. Remarkably, the diffraction peak (002) associated with RGO is identified at 20–30°, indicating the crumpled and partially stacked states of graphene layers after adjusting pH from 9 to 4. Raman spectrum of the $Fe_3O_4@RGO$ (Fig. 6b) shows a typical peak

of magnetite ~680 cm^{-1} and characteristic peaks of the D- and G-bands from graphene at around 1338 and 1600 cm^{-1}.

SEM was used to support the proposed self-assembly mechanism of $Fe_3O_4@GO$ sheets induced by PMAA, as well as showing the surface morphology of the resulting $Fe_3O_4@RGO$ anode after annealing treatment. Fig. 7a reveals a rough surface for PMMA-induced $Fe_3O_4@RGO$ materials. For comparison, the citric acid-stabilized $Fe_3O_4@RGO$ was analyzed under similar conditions and a clear contrast was observed, revealing a relatively smoother surface (Fig. 7b). Panels (c) and (d) of Fig. 7 clearly exhibit the porosity difference between PMAA-induced and citric acid-stabilized $Fe_3O_4@RGO$ anodes; the former shows more mesopores (~10–40 nm) than the latter. Furthermore, for PMAA-induced $Fe_3O_4@RGO$, there are fewer agglomerated Fe_3O_4 nanoparticles compared to those in the citric acid-stabilized $Fe_3O_4@RGO$ material. Additional SEM images of PMAA-induced $Fe_3O_4@RGO$ materials are presented in the Fig. S4.† The morphology of Fe_3O_4 particles on RGO sheets was characterized by high-resolution TEM image (Fig. S5†); the average size of Fe_3O_4 is ~10 nm with narrow size distribution.

To further investigate the porous structure and surface area of PMAA-induced $Fe_3O_4@RGO$ material, N$_2$ adsorption–desorption isotherms were obtained, as shown in Fig. 7e. The adsorption–desorption profile is close to type IV with an evident hysteresis loop in the 0.4–1.0 range of relative pressure, indicating the mesoporous structure of the $Fe_3O_4@RGO$ composites. In addition, the inset in Fig. 7e shows the pore-size distribution (obtained from the Barrett–Joyner–Halenda model) for PMAA-induced $Fe_3O_4@RGO$, in which the pore diameters are predominantly below ~10 nm. Therefore, it can be concluded that PMAA-induced $Fe_3O_4@RGO$ possesses a hierarchical porous structure composed of micropores and mesopores. Furthermore, the specific surface area of the composite is ~338.8 m^2 g^{-1}, which is clearly higher than many state-of-the-art $Fe_3O_4@RGO$ anodes reported in the literature (Table S1†).[12,28,37–39] To conclude, our porous structure of $Fe_3O_4@RGO$ material not only offers a buffer room for huge volume expansion of Fe_3O_4 during the charge/discharge cycles, but also facilitates the transport of lithium-ions and electrolyte molecules, which makes active sites accessible and eventually results in enhanced anode performance in LIBs.
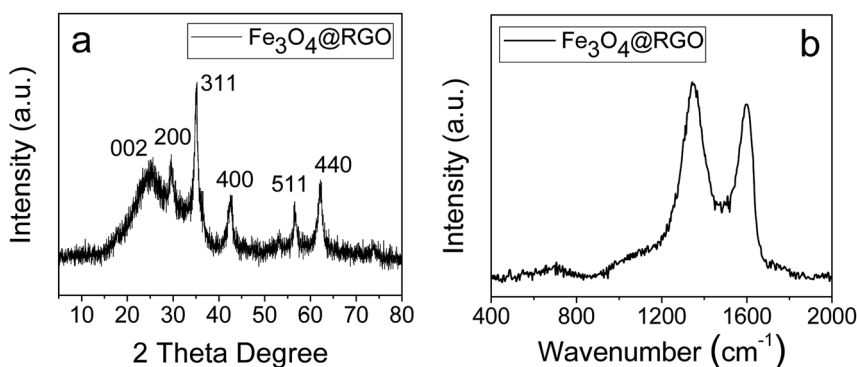

Fig. 6 (a) XRD pattern of $Fe_3O_4@RGO$. (b) Raman spectrum of $Fe_3O_4@RGO$.

Fig. 7 (a and b) SEM images of PMAA-induced porous Fe₃O₄@RGO. (c and d) Citric acid-assisted stacked Fe₃O₄@RGO. (e) Nitrogen adsorption–desorption isotherms and pore-size distribution of PMAA-induced porous Fe₃O₄@RGO (inset figure). (f) TGA curve of Fe₃O₄@RGO acquired with a temperature ramp of 5 °C min⁻¹ in air.

Electrochemical performance of Fe₃O₄@RGO anode

From the TGA data (Fig. 7f), the composition of Fe₃O₄ is ~60 wt%. Based on this weight ratio, the Fe₃O₄@RGO anode shows a theoretical capacity of ~703 mA h g⁻¹ (924 mA h g⁻¹ × 60 percent + 372 mA h g⁻¹ × 40 percent).[16] Fig. 8a shows the first four and the 200th charge–discharge curves of PMAA-induced Fe₃O₄@RGO half-

cell at a current density of 2 A g⁻¹, with a voltage window of 0.002–3.0 V. The first discharge capacity is about 1470 mA h g⁻¹, while the second capacity decreases to 770 mA h g⁻¹. The irreversible capacity loss is related to the formation of the solid-electrolyte interphase (SEI) film.[40,41] After 200 cycles, the capacity stabilizes at 480 mA h g⁻¹. For comparison, the citric acid-stabilized
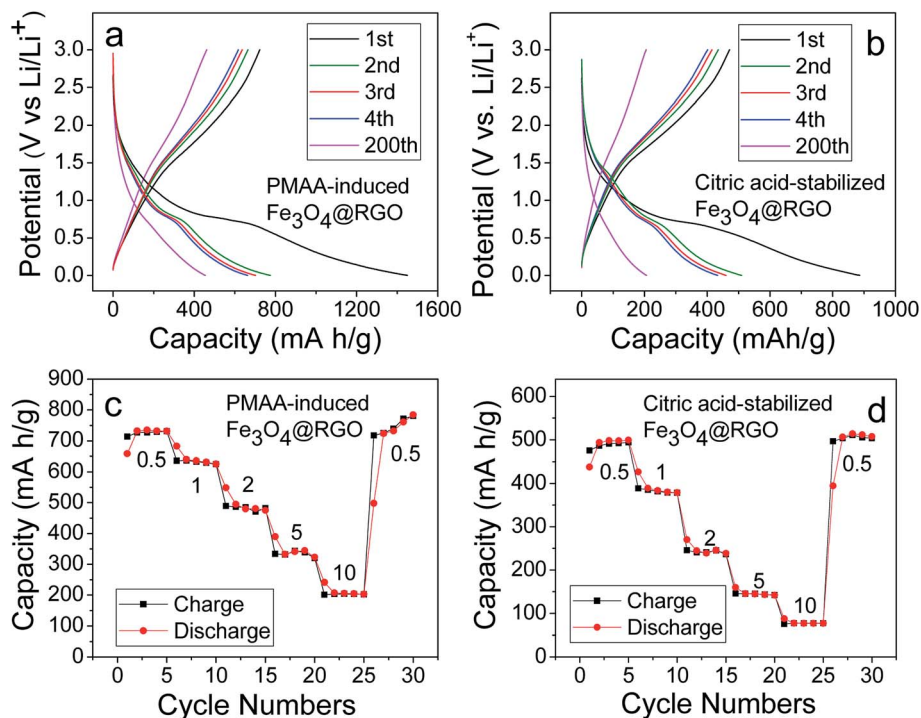
Fig. 8 (a) Selected discharge–charge profiles (1st, 2nd, 3rd, 4th, and 200th cycles) of a PMAA-induced Fe_3O_4/RGO anode, and (b) a citric acid-stabilized Fe_3O_4@RGO anode at a current density of 2 A g^{-1} in the potential window of 3.0–0.002 V (vs. Li/Li$^+$); (c) cycling performance of a PMAA-induced Fe_3O_4/RGO anode; and (d) a citric acid-stabilized Fe_3O_4@RGO anode at different cycling rates of 0.5 A g^{-1}, 1 A g^{-1}, 2 A g^{-1}, 5 A g^{-1}, and 10 A g^{-1} with a cutoff voltage window of 3.0–0.002 V.

Fe_3O_4@RGO anode is also cycled under the same conditions (Fig. 8b). It is obvious the specific capacity of citric acid-stabilized Fe_3O_4@RGO decreases faster than that of PMAA-induced Fe_3O_4@-RGO. The capacity gradually fades to 200 mA h g^{-1} during 200 discharge/charge cycles. Fig. S6† shows 1–100 cycling performance of PMAA-induced Fe_3O_4@RGO and citric acid-stabilized Fe_3O_4@-RGO anode at a low current rate (0.5 A g^{-1}), with the former showing superior performance. At this relatively lower cycling rate, the fading of capacities becomes slower for both samples compared to those at higher current (2 A g^{-1}).

The rate capability of PMAA-induced Fe_3O_4@RGO was studied at different current rates, from 0.5 to 10 A g^{-1} (Fig. 8c). Fig. 8c shows the decrease in the capacity with increasing C rates. A specific charge capacity of 740 mA h g^{-1} is obtained at 0.5 A g^{-1}, and even at a high current density of 10 A g^{-1}, it still delivers 200 mA h g^{-1}. In contrast, the capacity of citric acid-stabilized Fe_3O_4@RGO fades dramatically to 70 mA h g^{-1} at 10 A g^{-1} (Fig. 8d). In Fig. 8c, a high capacity of 780 mA h g^{-1} can be measured when the current rate reduces back from 10 A g^{-1} to 0.5 A g^{-1}, indicating a high stability as well as excellent reversibility. As shown in Fig. 9, the Li storage capacity of our Fe_3O_4@RGO is comparable to Fe_3O_4-based nanocarbon anodes with a higher weight percentage (69–89 wt%) of Fe_3O_4.[12,28,40–43] Fe_3O_4 shows a high theoretical capacity (924 mA h g^{-1}), therefore energy density of anodes is largely dependent on weight ratio of Fe_3O_4 to graphene or other nanocarbon component. However, excessive Fe_3O_4 in the anode often leaves it unprotected by

nanocarbon and inevitably exposed to the electrolyte, thus inducing volume expansion and capacity fading during the discharging/charging process. In this study, our anode composite only contains 60 wt% of Fe_3O_4, which enables the high energy density to be preserved while mitigating its structural pulverization. The improved stability and rate performance of the PMAA-induced Fe_3O_4@RGO is attributed to its hierarchical porous structure that facilitates fast Li$^+$ diffusion and an effective electron transport during the charge–discharge cycles.
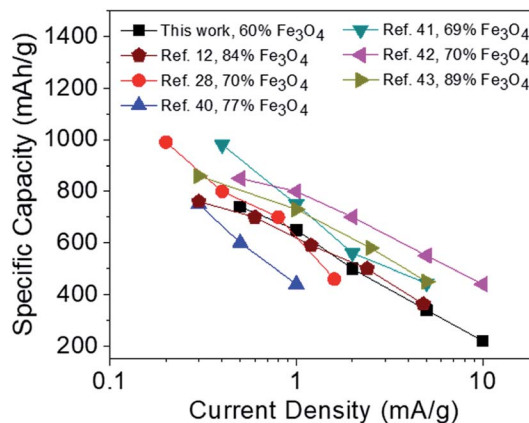

Fig. 9 Comparison of anode performance of Fe_3O_4@RGO with state-of-the-art Fe_3O_4-nanocarbons (containing different weight percentages of Fe_3O_4).

Conclusions

To summarize, our results elucidate the relationship between the media pH and nanomaterial structure, in terms of dispersion state of Fe_3O_4@GO and porosity of Fe_3O_4@RGO. By adjusting media pH, configuration and charge density of PMAA chains change, which largely determines the stability of Fe_3O_4@GO in water. The concentration ratio of PMAA and Fe_3O_4@GO plays another important role in the stability of Fe_3O_4@GO due to the 'bridging' phenomenon that dominates at different pH. The PMAA-induced self-assembly method is a facile method for designing high-performance Fe_3O_4@RGO anode materials. The presence of large amounts of mesopores improve the porosity of Fe_3O_4@RGO materials and provide buffer space for Fe_3O_4 particles, as well as accommodate the huge volume expansion during long-term discharge/charge cycles. The resulting Fe_3O_4@RGO anode with only 60 wt% Fe_3O_4 can still deliver high capacities of 740 mA h g^{-1} to 200 mA h g^{-1} at various current densities of 0.5 A g^{-1} to 10 A g^{-1}, which are comparable to other Fe_3O_4-based anodes with a higher weight ratio of Fe_3O_4. The PMAA-induced self-assembly method addresses the issue of poor dispersion of iron oxide-coated graphene materials and provides a highly porous graphene framework for depositing other higher-capacity active nanoparticles.

Experimental

Synthesis of PMAA

We added 150 ml of ethanol, 67 g of methacrylic acid (MAA), and 0.7 g of 2, 2′-azobis(2-methylpropionamidine) dihydrochloride (AIBA) to a 500 ml flask equipped with a thermocouple for monitoring the temperature and a mechanical stirring device. The reaction mixture was purged with argon at ambient temperature for 30 min under stirring. The temperature was then raised to 65 °C and the mixture was kept at 65 °C for 6 h. The reaction mixture was then cooled to 25 °C, and the sample was dried and stored for further analysis. The solid content (or percentage of PMAA) was ~35 wt% in the solvent.

Preparation of Fe_3O_4@GO–PMAA aqueous solution

The method for decoration of Fe_3O_4 nanoparticles on GO sheets is described in detail in our previous work.[16] We added 259.6 mg $FeCl_2 \cdot 4H_2O$ and 708.4 mg $FeCl_3 \cdot 4H_2O$ to GO dispersion (50 ml of 1 mg ml^{-1}) at 80 °C under N_2 atmosphere. For a lower weight ratio of PMAA to Fe_3O_4@GO composite, we mixed 12 mg of PMAA with 20 mg Fe_3O_4@GO in 10 ml water, and sonicated it at room temperature for 1 h to form coordinate bonds between Fe_3O_4 and PMAA; while for the sample with a higher ratio, we added 48 mg of PMAA in the dispersion. Ammonia and HCl solutions in water were used to adjust pH between 1 and 9 for the Fe_3O_4@GO–PMAA dispersed in water. In comparison, an Fe_3O_4@GO–citric acid dispersion was also prepared following the steps in our previous work.[16]

Self-assembly of porous Fe_3O_4@RGO anodes

The as-prepared Fe_3O_4@GO–PMAA dispersion (~2 ml) was drop-cast on the Cu current collector (9 μm thick) and dried at 40 °C in a vacuum oven. Thereafter, the dried Fe_3O_4/GO was annealed at 600 °C for 3 h in an argon atmosphere to reduce GO to RGO.[29] Synthesis steps for porous Fe_3O_4@RGO anodes are illustrated in Fig. 1. PMAA is able to stabilize Fe_3O_4@GO in water and facilitate the formation of a concentrated Fe_3O_4@GO dispersion (~2 mg ml^{-1}). Thereafter, by changing the pH of the solution from basic to acidic, crumpled Fe_3O_4@GO sheets were formed. An Fe_3O_4@RGO anode stabilized *via* citric acid treatment was also prepared for comparison.

Materials characterization

XRD patterns were collected on a Rigaku Miniflex II X-ray diffractometer with Cu Kα radiation (λ = 1.5418 Å) at 40 kV and 40 mA. The morphological characterization of the samples was conducted using a field-emission scanning electron microscope (SEM, Hitachi S5200) and a transmission electron microscope (TEM, FEI Talos). For TEM imaging, a small amount of the Fe_3O_4/RGO sample was dispersed in isopropanol *via* ultrasonication; a drop of the homogeneous suspension was deposited on a holey carbon TEM grid and examined at 120 and 200 kV. Thermogravimetric analysis (TGA) was performed on a Q500 TGA analyzer (TA Instruments) with a temperature ramp of 5 °C min^{-1} from room temperature (RT) to 900 °C under a stream of air flow for Fe_3O_4@RGO, and from RT to 600 °C under nitrogen flow for PMAA. UV-Vis measurements were performed on a UV-2600 spectrometer (Shimadzu) using plastic cuvettes. Suspensions were first diluted to a suitable value followed by four days of rest. The upper stable suspensions were finally used for UV-Vis measurements. Viscosity of the suspensions as a function of shear rate was measured using a Brookfield rheometer equipped with 40 mm parallel-plate geometry. The annealing treatment was performed in a chemical vapor deposition (CVD) system by heating it to 600 °C for 3 h in argon flow (250 sccm). Brunauer–Emmett–Teller (BET) specific surface areas were determined from N_2 adsorption using a Quantachrome (Autosorb-1) instrument at liquid nitrogen temperature. Raman spectra were measured using a Horiba 550 Raman spectrometer with a laser wavelength of 532 nm. The zeta potentials and effective particle sizes of Fe_3O_4@GO–PMAA were measured on a Brookhaven ZetaPALS analyzer. For reporting of accurate effective particle sizes, mean *z*-average diameter along with the standard deviations were derived based on seven replicate measurements. The pH dependence of zeta potential for Fe_3O_4@GO–PMAA aqueous suspension at 23 °C was measured at different pH values.

Electrochemical measurements

The half-cell assembly was carried out in an argon-filled glovebox with concentrations of moisture and oxygen below 5 ppm. The as-prepared Fe_3O_4@RGO nanocomposite on the Cu foil current collector was used as an anode for cells. The separator was a microporous polypropylene membrane and the counter electrode was Li foil. The electrolyte was prepared by dissolving 1 M of $LiPF_6$ in an ethylene carbonate (EC)/dimethyl carbonate (DMC)/diethyl carbonate (DEC) mixture (1 : 1 : 1, in wt%). The mass loading of anode materials was controlled around 4.6 mg cm^{-2} on the current

collector. Galvanostatic cycling experiments of the cells were performed on a Maccor 4300 battery test system in the voltage range of 0.001–3.00 V *versus* Li⁺/Li at room temperature.

Conflicts of interest

There are no conflicts to declare.

Acknowledgements

References

1 L. Zhai, *Chem. Soc. Rev.*, 2013, **42**, 7148–7160.
2 L. Qiu, D. Liu, Y. Wang, C. Cheng, K. Zhou, J. Ding, V. T. Truong and D. Li, *Adv. Mater.*, 2014, **26**, 3333–3337.
3 C. De las Heras Alarcón, S. Pennadam and C. Alexander, *Chem. Soc. Rev.*, 2005, **34**, 276–285.
4 G. D. Mendenhall, Y. Geng and J. Hwang, *J. Colloid Interface Sci.*, 1996, **184**, 519–526.
5 X. Wang, X. Ye and G. Zhang, *Soft Matter*, 2015, **11**, 5381–5388.
6 J. Zhang and N. A. Peppas, *Macromolecules*, 2000, **33**, 102–107.
7 M. R. de Moura, F. A. Aouada and L. H. Mattoso, *J. Colloid Interface Sci.*, 2008, **321**, 477–483.
8 K. C. Etika, M. A. Cox and J. C. Grunlan, *Polymer*, 2010, **51**, 1761–1770.
9 K. Wu, H. Yang, L. Jia, Y. Pan, Y. Hao, K. Zhang, K. Du and G. Hu, *Green Chem.*, 2019, **21**, 1472–1483.
10 K. Wu, K. Du and G. Hu, *J. Mater. Chem. A*, 2018, **6**, 3444–3453.
11 K. Wu, D. Liu and Y. Tang, *Electrochim. Acta*, 2018, **263**, 515–523.
12 W. Wei, S. Yang, H. Zhou, I. Lieberwirth, X. Feng and K. Müllen, *Adv. Mater.*, 2013, **25**, 2909–2914.
13 H. Wei, W. Yang, Q. Xi and X. Chen, *Mater. Lett.*, 2012, **82**, 224–226.
14 X. Zhao, L. Yang, X. Li, X. Jia, L. Liu, J. Zeng, J. Guo and P. Liu, *Bioconjug. Chem.*, 2015, **26**, 128–136.
15 T. Gao, Q. Ye, X. Pei, Y. Xia and F. Zhou, *J. Appl. Polym. Sci.*, 2013, **127**, 3074–3083.
16 H. Wang, J. Xie, M. Follette, T. C. Back and P. B. Amama, *RSC Adv.*, 2016, **6**, 83117–83125.
17 H. Wang, X. Li, M. Baker-Fales and P. B. Amama, *Curr. Opin. Chem. Eng.*, 2016, **13**, 124–132.
18 C. Kibby, K. Jothimurugesan, T. Das, H. S. Lacheen, T. Rea and R. J. Saxton, *Catal. Today*, 2013, **215**, 131–141.
19 L. Li, A. Kovalchuk, H. Fei, Z. Peng, Y. Li, N. D. Kim, C. Xiang, Y. Yang, G. Ruan and J. M. Tour, *Adv. Energy Mater.*, 2015, **5**, 1500171–1500176.
20 L. Zhao, M. Gao, W. Yue, Y. Jiang, Y. Wang, Y. Ren and F. Hu, *ACS Appl. Mater. Interfaces*, 2015, **7**, 9709–9715.
21 X. Fan, S. Li, H. Zhou and L. Lu, *Electrochim. Acta*, 2015, **180**, 1041–1049.
22 M. Zhang and M. Jia, *J. Alloys Compd.*, 2013, **551**, 53–60.
23 M. Ren, M. Yang, W. Liu, M. Li, L. Su, C. Qiao, X. Wu and H. Ma, *Electrochim. Acta*, 2016, **194**, 219–227.
24 Y. Chen, B. Song, L. Lu and J. Xue, *Nanoscale*, 2013, **5**, 6797–6803.
25 L. Li, P. Gao, S. Gai, F. He, Y. Chen, M. Zhang and P. Yang, *Electrochim. Acta*, 2016, **190**, 566–573.
26 D. Chen, G. Ji, Y. Ma, J. Y. Lee and J. Lu, *ACS Appl. Mater. Interfaces*, 2011, **3**, 3078–3083.
27 S. H. Choi and Y. C. Kang, *Carbon*, 2014, **79**, 58–66.
28 J. Su, M. Cao, L. Ren and C. Hu, *J. Phys. Chem. C*, 2011, **115**, 14469–14477.
29 H. Wang, J. Xie, H. Almkhelfe, V. Zane, R. Ebini, C. Sorensen and P. B. Amama, *J. Mater. Chem. A*, 2017, **5**, 23228–23237.
30 S. Yu and G. M. Chow, *J. Mater. Chem.*, 2004, **14**, 2781–2786.
31 M. Zembala, *Adv. Colloid Interface Sci.*, 2004, **112**, 59–92.
32 P. K. Koutsoukos, P. G. Klepetsanis and N. Spanos, *Zeta-Potential Calculation*, CRC Press, 2016.
33 J. C. Grunlan, L. Liu and O. Regev, *J. Colloid Interface Sci.*, 2008, **317**, 346–349.
34 A. Ditsch, P. E. Laibinis, D. I. Wang and T. A. Hatton, *Langmuir*, 2005, **21**, 6006–6018.
35 J. Xiao, Y. Tan, Y. Song and Q. Zheng, *RSC Adv.*, 2016, **6**, 41392–41403.
36 C. Robin, C. Lorthioir, C. Amiel, A. Fall, G. Ovarlez and C. Le Cœur, *Macromolecules*, 2017, **50**, 700–710.
37 N. A. Zubir, C. Yacou, J. Motuzas, X. Zhang and J. C. D. Da Costa, *Sci. Rep.*, 2014, **4**, 4594.
38 X. Li, X. Huang, D. Liu, X. Wang, S. Song, L. Zhou and H. Zhang, *J. Phys. Chem. C*, 2011, **115**, 21567–21573.
39 Z.-S. Wu, S. Yang, Y. Sun, K. Parvez, X. Feng and K. Müllen, *J. Am. Chem. Soc.*, 2012, **134**, 9082–9085.
40 P. Lian, X. Zhu, H. Xiang, Z. Li, W. Yang and H. Wang, *Electrochim. Acta*, 2010, **56**, 834–840.
41 Z. Zhang, F. Wang, Q. An, W. Li and P. Wu, *J. Mater. Chem. A*, 2015, **3**, 7036–7043.
42 S. Hao, B. Zhang, Y. Wang, C. Li, J. Feng, S. Ball, M. Srinivasan, J. Wu and Y. Huang, *Electrochim. Acta*, 2018, **260**, 965–973.
43 L. Jun, X. Xijun, H. Renzong, Y. Lichun and Z. Min, *Adv. Energy Mater.*, 2016, **6**, 1600256.